Application of First-Principles Sequential Inversion in Geotechnical Engineering: An Engineering Framework for Predicting Tunnel-Induced Ground Deformation

Zhengyong Wei[1,2]
[1]*Department of Civil Engineering, School of Future Transportation, Guangzhou Maritime University, Guangzhou, China*
[2]*Guangzhou Jiao Tong University (preparatory), Guangzhou, China*

doi: https://doi.org/10.21467/proceedings.8.2.14

ABSTRACT

Mechanised tunnelling induces ground deformation under sparse, stage-dependent monitoring, where soft-penalty surrogates and purely data-driven models risk physically inadmissible extrapolation. This study proposes a First-Principles Sequential Inversion (FPSI) framework that encodes governing mechanics as inviolable hard constraints within a sequential maximum-a-posteriori (MAP) scheme. Mechanics-derived constitutive relations, including Terzaghi one-dimensional consolidation with Mesri–Godlewski secondary compression and the Euler–Bernoulli beam-on-elastic-foundation, are integrated with the semi-empirical Peck Gaussian settlement trough whose parameters are strictly confined to geotechnically admissible bounds. Site-informed physical priors, stage monotonicity enforcement via bounded L-BFGS-B optimisation, and clipped residual-bias correction collectively preserve admissibility throughout inversion, while a stage-wise risk index closes the monitoring-to-decision loop without post-processing validation across three Greater Bay Area projects demonstrates consistent transferability. Guangzhou Metro Line 8 recovers Peck parameters with $R^2 \geq 0.942$ and RMSE ≤ 0.269 mm across four SNR-adequate stages, with an 86% monotonic reduction in volume loss. Shenzhen Metro Line 13 reproduces longitudinal FBG profiles with $R^2 \geq 0.942$ and RMSE ≤ 1.06 mm, with transverse inversion yielding $K = 0.221$ consistent with stiff granitic overburden. The Hong Kong-Zhuhai-Macau Bridge immersed tunnel recovers grouting efficiency $\eta = 0.45$–0.54 within the reported 40%–67% range, with the risk index peaking at year 3, two years before the 50 mm serviceability threshold was breached at year 5. FPSI framework provides a physically interpretable, sequentially updating inversion scheme that generates real-time risk alerts under the sparse monitoring conditions characteristic of staged mechanised construction.

1 INTRODUCTION

Urban metro expansion in the Greater Bay Area (GBA) and other high density cities increasingly forces mechanised shield tunnels to pass within metres of pile supported structures. Excavation induced volume loss, stress redistribution, and pore pressure transients generate coupled ground–pile responses that may approach serviceability limits. Reliable real time prediction is therefore essential for risk informed construction management and early warning. The principal constraint on any predictive framework is data scarcity rather than model complexity. Field monitoring is typically sparse and stage dependent. Purely data driven methods can interpolate well but often give physically inconsistent extrapolations when observations are limited (Yuan *et al.* 2025). High fidelity three dimensional finite element analyses provide mechanistically complete benchmarks but cannot be updated online without repeated recalibration. These limitations motivate a framework that combines the physical interpretability of classical analytical solutions with the sequential updating capability of Bayesian parameter inversion. Recent physics informed developments include an extreme learning machine for soil–pile interaction (Guo *et al.* 2025), a physics–data dual driven model for twin shield settlement (Hu *et al.* 2026), and a dynamic framework that integrates simulation with data driven correction for railway tunnels (Wang *et al.* 2024). However, most existing approaches enforce physics as soft penalty terms during training, so constraint admissibility at inference time remains unresolved.

The present study addresses this gap through a First-Principles Sequential Inversion (FPSI) framework with three core characteristics:

(a) Classical analytical solutions, including the Peck trough, Terzaghi consolidation theory, and the beam-on-elastic-foundation formulation, are embedded as hard constraints through inviolable parameter bounds and

© 2026 Copyright held by the author(s). Published by AIJR Publisher in " Proceedings of The HKIE Geotechnical Division 46th Annual Seminar 2026: Bridging Theory and Practice in Geotechnical Engineering" (GDAS2026). Organized by the Geotechnical Division, The Hong Kong Institution of Engineers, Hong Kong on May 12, 2026.

Proceedings DOI: 10.21467/proceedings.8.2; Series: AIJR Proceedings; ISSN: 2582-3922; ISBN: 978-81-688301-1-0

residual feasibility conditions, in contrast to soft-penalty regularisation approaches that permit boundary violations.

(b) Parameters are updated one construction stage at a time, with each stage posterior serving as the prior for the next.This warm-start design is matched to the episodic nature of construction monitoring.

(c) Inverted parameters map directly to normalised risk indices referenced to pre-defined alert thresholds, completing the monitoring-to-decision loop without post-processing.

2 Methodology: First-Principles Sequential Inversion (FPSI) Framework

2.1 Problem formalization: states–parameters–observations

To enable a monitoring-driven and physically auditable representation of tunnel soil–pile interaction, the construction-stage system is formulated in a state–parameter–observation form that separates (i) the evolving system response, (ii) latent geotechnical drivers, and (iii) heterogeneous measurements. Let x_k denote the system state at construction stage k collecting the primary response variables governing safety-relevant behaviour, including ground displacement fields, pore-pressure response, and pile kinematics, from which structural response quantities may be derived. Let θ_k represent the latent parameter vector controlling the coupled response but not directly observable in routine construction monitoring, including model-specific quantities such as effective stiffness, compressibility, ground-loss surrogates, grouting efficiency, soil–pile coupling stiffness, and consolidation-related time scales. Observations are denoted by y_k, comprising multi-source monitoring streams such as settlement markers, lateral displacement measurements, structural inclination, strain- or curvature-derived indicators, pore pressure, and auxiliary operational logs.

$$x_{k+1} = f(x_k, u_k, \theta_k) + w_k, y_k = h(x_k) + v_k \tag{1}$$

where u_k denotes construction control inputs such as face pressure, advance rate, and grouting parameters, while w_k and v_k represent process uncertainty and measurement noise, respectively. The system evolution operator $f(\bullet)$ is explicitly defined by first-principles geomechanical models governing excavation-induced ground response. The observation operator $h(\bullet)$ maps the latent system state and parameters to measurable quantities recorded by the monitoring system, including surface settlement markers, fibre Bragg grating sensors, inclinometers, and piezometers.

2.2 Core Mechanistic Model

In this study, a set of core mechanistic models is adopted to describe the key processes governing tunnel–ground interaction. These low-dimensional formulations balance physical interpretability with empirical robustness, allowing model parameters to be directly updated from field monitoring data and providing a stable basis for sequential data assimilation and uncertainty quantification. Model selection follows a principle of minimal sufficiency, retaining dominant mechanisms controlling excavation-induced deformation and settlement while minimising superfluous parameters. This parsimonious approach enhances transparency and numerical stability, enabling robust parameter inference under sparse, noisy monitoring typical of soft-soil tunnelling environments.

2.2.1 Ground deformation: Peck Gaussian trough

Given a disturbance driver, the ground response is expressed as a parameterised displacement field that is computable and monitoring-consistent. For settlement-dominated indicators, the Gaussian trough remains a robust workhorse for greenfield surface settlement. In the present 3D setting, k denotes the longitudinal station (e.g., ring index/chainage), so three-dimensionality is captured through the *k-dependence* of the trough amplitude and width. The surface settlement at transverse offset x is written as

$$s(x;k) = s_{\max}(k)\exp\left(-\frac{x^2}{2i^2(k)}\right) \tag{2}$$

where $S_{max}(k)$ denotes the peak settlement and $i(k)$ is the settlement-trough width parameter. In line with classical tunnelling practice, $S_{max}(k)$ can be related to the volume loss through a mass-conservation argument,

Proceedings DOI: 10.21467/proceedings.8.2
ISBN: 978-81-688301-1-0

Series: AIJR Proceedings
ISSN: 2582-3922

while *i(k)* is commonly parameterised as a function of tunnel depth and ground conditions, for example $\left(i = Kz_0\right)$, with *K* treated as a site-specific parameter to be calibrated. (Peck, 1969; O'Reilly and New, 1982; Mair *et al*., 1996)

$$s_{max}(k) = \frac{V_L A_{exc}(k)}{\sqrt{2\pi}\, i(k)} \tag{3}$$

$$i(k) = Kz_0(k) \tag{4}$$

For pile assessment, lateral ground movement can be as influential as settlement because it governs pile curvature and bending demand. A convenient choice is therefore to parameterise the transverse lateral displacement in a manner consistent with the settlement trough, using the same low-dimensional controls. One such representation expresses lateral movement as proportional to the transverse gradient of settlement, which naturally yields zero displacement at the centreline and peak values on the flanks of the trough:

$$u(x;k) = \alpha(k)\frac{\partial s(x;k)}{\partial x} \tag{5}$$

where $\alpha(k)$ is a dimensionless coupling coefficient that aggregates soil type, drainage regime, and 3D deformation effects (including longitudinal variability embedded in $S_{\max}(k)$ and $i(k)$), and it is treated as an inferable parameter when lateral monitoring is available.

The deformation accumulation function $g(t;\tau)$ maps elapsed construction time *t* to the fractional development of settlement, and is required to be monotonically non-decreasing and bounded on [0, 1]. A logistic-sigmoid form is adopted:

$$g(t;\tau,t_{50}) = \frac{1}{1+\exp(-\frac{t-t_{50}}{\tau})} \tag{6}$$

where t_{50} is the time at which 50 percent of the ultimate settlement is reached, and $\tau>0$ is a transition scale parameter that controls the rate of deformation development. This logistic form is monotonic and bounded by construction and approaches a Heaviside step function as τ becomes small. We treat both t_{50} and τ as inferable parameters in the sequential MAP scheme, and we assign priors based on the advance rate and grouting records.

Pore-pressure evolution is considered when the ground is partially or fully saturated and consolidation effects are material. At the core-model level, the excess pore pressure u_e is represented by a diffusion-type governing equation, augmented with a source term that captures excavation- and grouting-induced disturbances.

$$\frac{\partial u_e}{\partial t} = c_v \nabla^2 u_e + q(x,z,t) \tag{7}$$

where C_v is the coefficient of consolidation and *q* denotes a disturbance-induced source term or boundary flux. Together, the deformation components (*s,u*) and the excess pore pressure u_e constitute a minimal state description that couples excavation actions to ground response and, in turn, to pile behaviour in a manner consistent with field monitoring.

2.2.2 Soil – pile interaction and pile body response

Soil–pile interaction is formulated through displacement compatibility and load transfer, so that the mapping from ground movement to pile response remains explicit, physically interpretable, and amenable to calibration. The lateral response is modelled by an Euler–Bernoulli pile on an elastic foundation, with the ground lateral displacement $u_s(z,k)$ entering as an imposed kinematic field,

$$EI\frac{d^4 u_p}{dz^4} + k_h(z)\left(u_p(z,k) - u_s(z,k)\right) = 0 \tag{8}$$

Here u_p denotes pile lateral deflection, *EI* is the flexural rigidity, and $k_h(z)$ is the depth-dependent subgrade reaction modulus that may reflect stratification. Internal-force observables follow directly from beam theory, with bending moment $M(z,k) = -EId^2u_p/dz^2$ and shear force $V(z,k) = -EId^3u_p/dz^3$.Importantly, this representation supports parameter inversion because $k_h(z)$ can be regularised into a low-dimensional profile and updated using measurements such as pile-head displacement and rotation, inclinometer-derived deflection profiles, or strain-based curvature reconstructed from distributed sensing.

Axial response is driven by relative vertical movement between the pile and the settling ground, which may mobilise negative skin friction, induce dragload, and shift the neutral plane. A minimal load-transfer formulation expresses axial equilibrium as

$$\frac{dN}{dz} + 2\pi r\tau(z,k) = 0, \tau = \tau\left(s(z,k) - w_p(z,k)\right) \tag{9}$$

where N is axial force, r is pile radius,w_p is pile axial displacement, and τ is the mobilised shaft resistance governed by the local relative slip. While the detailed t–z relation may be selected according to available site characterisation, the key requirement for the digital-twin workflow is that it introduces identifiable parameters, such as mobilisation stiffness and limiting shaft resistance, that admit physically informed priors and can be updated when strain-derived axial force measurements are available.

2.2.3 Long-term consolidation with secondary compression

Long-term settlement in soft clay deposits is governed by primary consolidation and subsequent creep deformation. The primary consolidation process is described using the classical one-dimensional theory of Karl von Terzaghi, in which settlement evolves as

$$s_p(t) = s_{\text{final}}(1-\eta)U(T_v), T_v = \frac{c_v t}{H_{dr}^2} \tag{10}$$

where c_v is the coefficient of consolidation, H_{dr} is the drainage path length, and $U(T_v)$ is the average degree of consolidation obtained from the standard series solution. η represents the grouting efficiency of synchronous shield tail grouting. This formulation captures the diffusion-controlled dissipation of excess pore pressure and provides a physically interpretable description of time-dependent settlement.

However, extensive field monitoring in soft marine and alluvial clays has consistently shown that settlement may continue beyond the completion of primary consolidation due to time-dependent creep of the soil skeleton. To capture this well-documented behaviour, an additional secondary compression component is incorporated following the formulation proposed by Mehmet Mesri and Peter Godlewski (1977):

$$\Delta s_{\text{sec}}(t, t_{EOP}) = C_\alpha H_{dr} \log_{10}\left(\frac{t}{t_{EOP}}\right), t > t_{EOP} \tag{11}$$

where C_α denotes the secondary compression index and t_{EOP} represents the end of primary consolidation.
A suitable expression for the time-dependent settlement therefore takes the form:

$$s(t) = s_p(t) + \Delta s_{\text{sec}}(t) \tag{12}$$

which represents the superposition of primary consolidation and subsequent creep deformation. This formulation provides a compact yet physically interpretable description of the full settlement evolution. Because the governing parameters (c_v ,H_{dr} ,C_α) correspond directly to standard geotechnical properties routinely obtained from laboratory or field characterisation, the model remains identifiable and transferable across a wide range of soft-soil conditions. The physically meaningful parameterisation further enables sequential updating using field monitoring data, making the approach well suited for long-term settlement prediction within monitoring-informed digital twin frameworks.

2.3 Sequential MAP Inversion

The parameter estimation at stage $\boldsymbol{k}$ is formulated as the minimisation of the following objective function:

$$J_k(\theta) = \sum_i w_i \| y_{k,i} - g_{k,i}(\theta)\|^2 + (\theta - \theta_0)^T P_0^{-1}(\theta - \theta_0) + \mu(\theta - \theta_{k-1}^*)^T \Delta^{-1}(\theta - \theta_{k-1}^*) \tag{13}$$

the first term represents the weighted data misfit, the second term incorporates geotechnically informed parameter priors, and the third term enforces temporal smoothness between consecutive construction stages to suppress non-physical parameter oscillations.θ denotes the parameter vector to be estimated at the current stage, and $\theta_{k-1}^*$is the optimal parameter vector obtained at the previous stage. $y_{k,i}$ represents the monitoring observation i at stage k, while $g_{k,i}(\theta)$ denotes the corresponding model prediction. The weights w_i account for measurement reliability and are set to 1.0 under normal construction conditions and reduced to 0.5 for epochs flagged as anomalous in the construction log. The vector θ_0 contains the prior parameter means derived from site investigation reports, and P_0^{-1} is the diagonal precision matrix constructed from the inverse prior variances. The matrix Δ controls the smoothness penalty applied to stage-to-stage parameter variation. For parameters expected to evolve monotonically (e.g., V_L and S_{final}), the corresponding entries of Δ are set equal

Proceedings DOI: 10.21467/proceedings.8.2
ISBN: 978-81-688301-1-0

Series: AIJR Proceedings
ISSN: 2582-3922

to their prior variances, whereas parameters affected by discrete grouting interventions are exempted from the smoothness constraint at the intervention stage.

The optimisation problem is solved using the L-BFGS-B algorithm, which enforces parameter bounds during each line-search step. Successive stages are initialised using a warm start from θ_{k-1}^{*}, reducing the number of iterations from approximately 200–500 for a cold start to 40–120 across all cases.

Parameter uncertainty is quantified by approximating the posterior covariance using the inverse numerical Hessian evaluated at the optimum:

$$\Sigma_k \approx \left[\nabla_\theta^2 J_k(\theta_k^*)\right]^{-1} \tag{14}$$

The Hessian is computed using second-order central finite differences with a step size proportional to the magnitude of each parameter. Negative curvature directions caused by numerical noise are regularised with a small positive floor to ensure positive definiteness. A total of 2000 samples are then drawn from the Gaussian approximation $\boldsymbol{N}(\theta_k^*, \Sigma_k)$ and projected onto the admissible parameter domain. The resulting bootstrap ensemble captures boundary-induced asymmetry and propagates parameter uncertainty into downstream deformation forecasts and risk indicators.

2.4 Residual Bias Correction

Despite the first-principles parameterisation, residual model–data discrepancy can arise from three-dimensional effects, anisotropy, or unmodelled construction events. A bounded multiplicative factor absorbs this discrepancy while preserving physical admissibility:

$$b(k) = \mathrm{clip}_{[-b_{\max}, +b_{\max}]}\left(\frac{y_{\mathrm{obs}}(k) - y_{\mathrm{phys}}(k)}{y_{\mathrm{phys}}(k)}\right), \hat{s}(k) = y_{\mathrm{phys}}(k)\cdot[1 + b(k)] \tag{15}$$

with b_{max} = 0.15,corresponding to the maximum residual discrepancy observed across the three case studies under physically consistent parameter estimates, and consistent with the ±15% tolerance widely adopted in geotechnical back-analysis to separate model inadequacy from measurement scatter (Mair *et al.* 1996). Any computed $|b|$ exceeding this threshold is treated as evidence of an unmodelled mechanism and flagged for manual review rather than silently absorbed. The correction differs fundamentally from a machine-learning residual: it has no trained weights, requires no held-out data, and is evaluated in closed form.

2.5 Stage-Wise Risk Index

The risk index maps the primary risk-driving parameter directly to a normalised alert level:

$$\mathrm{R}(k) = \min\left[1, \frac{|\theta_{\mathrm{risk}}(k)|}{\theta_{\mathrm{threshold}}}\right] \tag{16}$$

where $\theta_{\mathrm{risk}}(k)$ denotes the stage-dependent parameter controlling serviceability risk, and $\theta_{\mathrm{threshold}}$ represents the corresponding site-specific serviceability limit obtained from design specifications or project monitoring guidelines. For shield-tunnelling cases , the risk-driving parameter is the volume-loss coefficient V_L; For consolidation-dominated settlement, it is the final settlement parameter s_{final}.

The resulting index ranges from 0 to 1 and is directly linked to two predefined operational alert levels. Level $L1$ ($\mathscr{R}(k) \geq 0.50$) indicates elevated risk and triggers construction advisory together with increased monitoring frequency. Level $L2$ ($\mathscr{R}(k) \geq 0.80$) indicates a high-risk condition and requires temporary construction suspension followed by geotechnical review.

3 Case Study: Guangdong-Hong Kong-Macao Greater Bay Area Tunnel Projects

The FPSI framework was validated using distilled monitoring data from three representative GBA projects: (A) Guangzhou Metro Line 8 (Tongdewei–Shangbu Section; upper-soft lower-hard composite strata), (B) Shenzhen Metro Line 13 (Keyuan–Shenzhen University section; silty clay with documented longitudinal settlement monitoring), and (C) Hong Kong–Zhuhai–Macao Bridge immersed tunnel (marine Holocene clay with joint grouting).The cases span urban shield tunnelling and marine immersed tunnelling, with burial depths of 14–45 m and diameters of 6–15 m.Subsurface conditions include soft clays (c = 10–30 kPa; E = 5–50 MPa), silty clay, and weathered granite, covering a broad stiffness and boundary spectrum.

The global smoothness weight μ in Eq (13) is fixed at 0.5 based on leave-one-out cross-validation using Case A and is kept constant for all case studies.All numerical simulations and statistical analyses were implemented in Python 3.12.0 within a fully reproducible computational environment, ensuring transparency, portability, and methodological consistency across inversion, optimization, and diagnostic procedures.

3.1 Guangzhou Metro Line 8: Physics Benchmark (Tongdewei–Shangbu Section; upper-soft lower-hard composite strata)

3.1.1 Project Overview & Experiment Setup

The Tongdewei–Shangbu section of Guangzhou Metro Line 8, part of the 16.3 km northern extension in Guangzhou, consists of twin slurry-shield tunnels with a total length of 617 m. The tunnels have an outer lining diameter of 6.0 m, an inner diameter of 5.4 m, and a lining thickness of 0.30 m. The typical crown depth is approximately 14 m, ranging from 10 to 16 m according to Lv *et al.* (2020). The excavation cross-sectional area is 28.27 m².The alignment passes through a representative upper-soft and lower-hard stratigraphic profile typical of the Guangdong–Hong Kong–Macao Greater Bay Area. The upper layers consist of fill, silty clay, and sand, underlain by residual soil and slightly weathered limestone. This stratigraphy produces pronounced stiffness contrasts. The soft soils have cohesion values of about 8 to 15 kPa and an initial deformation modulus of roughly 2.5 MPa, whereas the limestone has a modulus of approximately 10 GPa. The resulting hard-rock height ratio β varies from 0 to 1 along the alignment, as reported by Lv *et al.* (2020).

This case provides a physics-based benchmark for model validation. Peak settlements reported by Lv *et al.* (2020) are used to anchor the Peck settlement trough across five excavation progress ratios β. Transverse settlement profiles are synthesised by superimposing spatially correlated AR(1) noise with a standard deviation σ = 0.25 mm and correlation coefficient ρ = 0.35 to emulate instrument scatter. The objective is to verify the ability of the FPSI framework to recover the key Peck parameters under realistic measurement noise, which is a prerequisite for deployment in real monitoring scenarios. Parameter bounds are defined as $K \in [0.20, 0.65]$ and $V_L \in [0.001, 0.025]$. The prior means are $\mu_K = 0.40$ with $\sigma_K = 0.10$ and $\mu_{VL} = 0.010$ with $\sigma_{VL} = 0.005$, while the regularisation weight is set to $\lambda = 0.25$.

3.1.2 Simulation Result &Conclusion

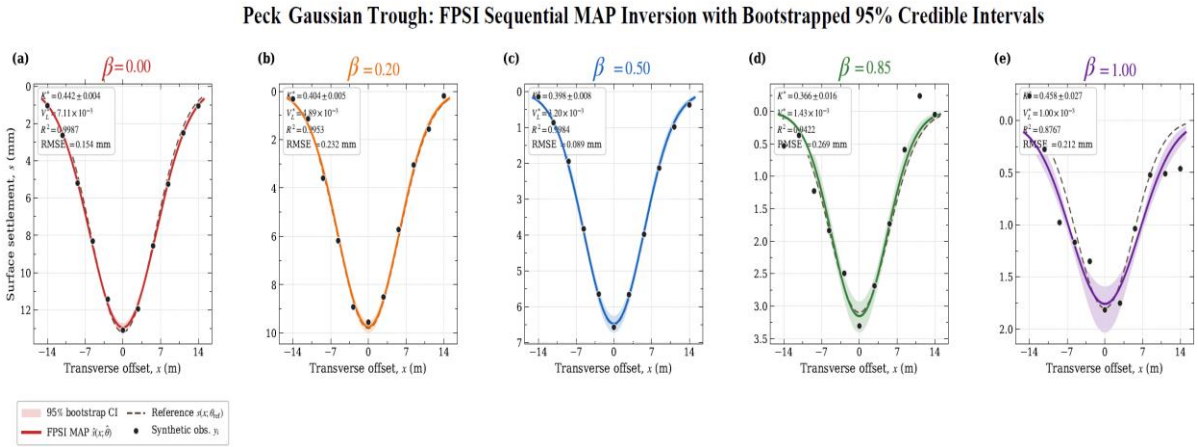


Figure 1. Transverse settlement profiles at five excavation progress stages.

Proceedings DOI: 10.21467/proceedings.8.2
ISBN: 978-81-688301-1-0

Series: AIJR Proceedings
ISSN: 2582-3922

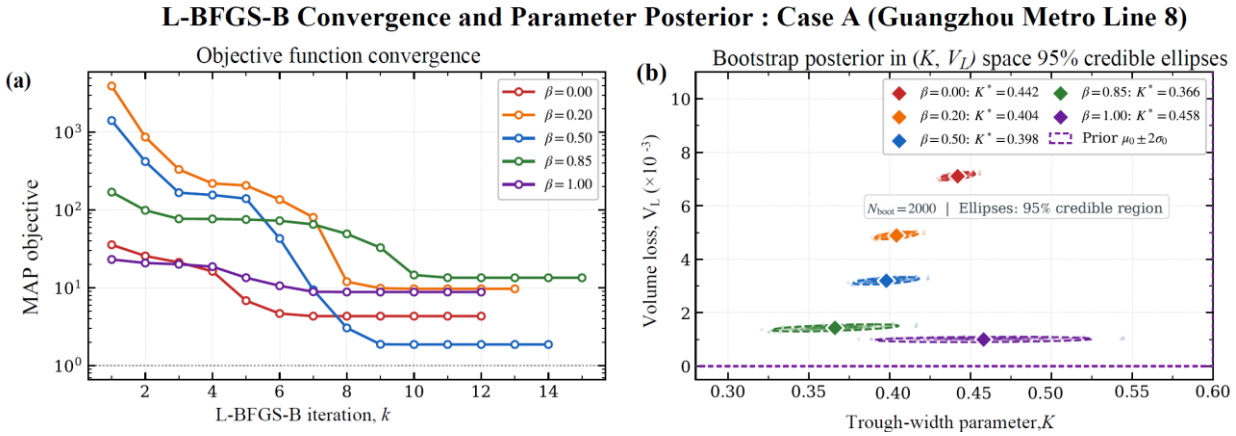


Figure 2. (a) MAP objective trajectories for five cross-sections; each curve records actual L-BFGS-B iterations. (b) Parametric bootstrap posterior distributions in the (K, V_L) plane,ellipses are 95% credible regions from the numerical Hessian.

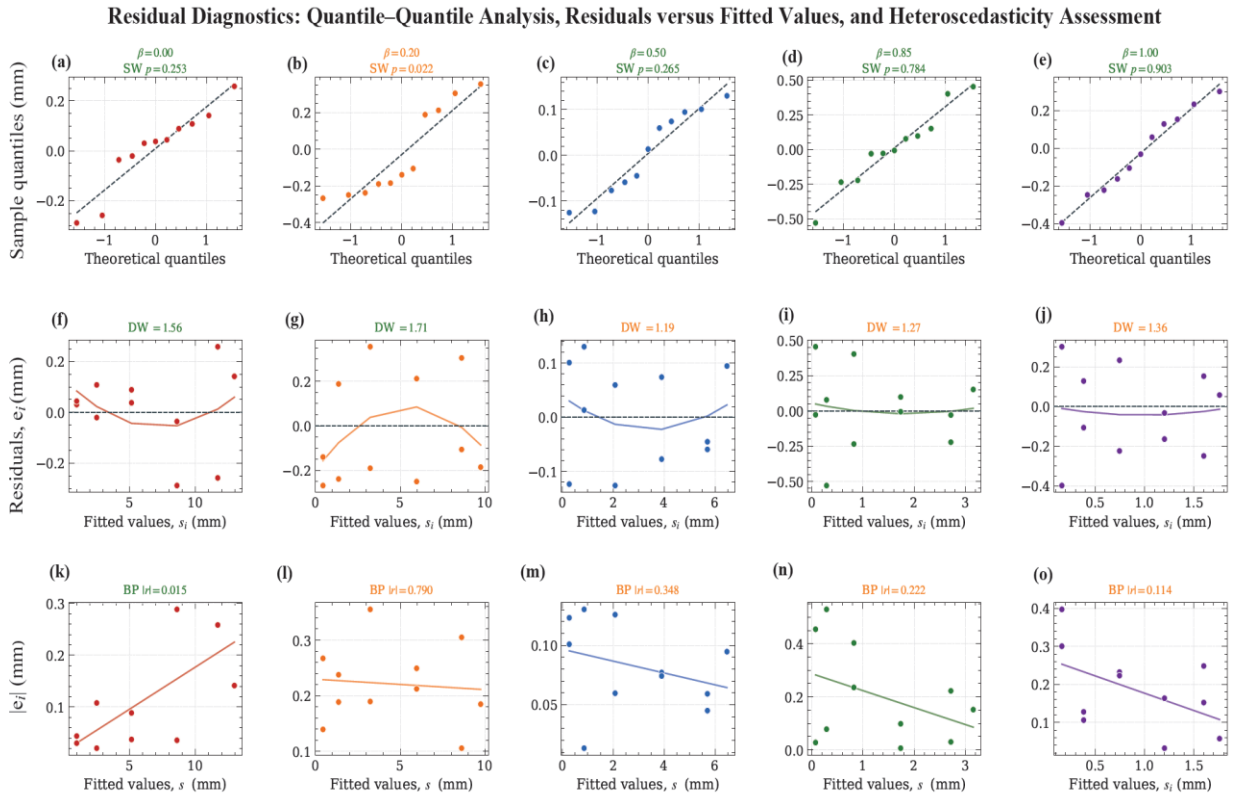


Figure 3. Residual diagnostics for all five sections: (a–e) normal Q–Q plots with Shapiro–Wilk p-values; (f–j) residuals versus fitted values with quadratic trend and Durbin–Watson statistic d; (k–o) absolute residuals versus fitted values for heteroscedasticity assessment.

Table 1: Stage-wise Inversion and Model Diagnostics

β	K^*	σ_K	V_L^*	σ_{v_L}	R^2	*adj.* R^2	RMSE (mm)
0	0.442	0.004	7.11	0.061	0.999	0.998	0.154
0.2	0.404	0.005	4.89	0.057	0.995	0.994	0.232
0.5	0.398	0.008	3.2	0.057	0.998	0.998	0.089
0.85	0.366	0.016	1.43	0.055	0.942	0.928	0.269
1	0.458	0.027	1	0.04	0.877	0.846	0.212

Note: β denotes the hard-rock height ratio; K^* is the trough-width coefficient describing the lateral extent of the settlement trough; σ_K represents the standard deviation of K^*, indicating the uncertainty in trough width; V_L^* is the volume loss ($\times 10^{-3}$) associated with tunnelling-induced ground deformation; σ_{V_L} denotes the standard deviation of V_L^*; R^2 and *adj.* R^2 are the coefficient of determination and the adjusted coefficient of determination, respectively; RMSE is the root-mean-square error of the model prediction (mm);

The FPSI framework recovers physically admissible Peck trough parameters K and V_L at all five excavation stages under AR(1) instrument noise (σ = 0.25 mm, ρ = 0.35). As shown in Figure 1 and Table 1, predictive accuracy is high for $\beta \leq 0.85$, with $R^2 \geq 0.942$ and RMSE ≤ 0.269 mm across those four stages.The marginal decline at β = 1.00 (R^2 = 0.877, RMSE = 0.212 mm) arises from a signal-to-noise ratio of approximately 7.2, indicating a limitation of the data rather than a deficiency in the framework.Volume loss decreases monotonically from $V_L^* = 7.11 \times 10^{-3}$ at $\beta = 0$ to 1.00×10^{-3} at β = 1.00, an 86% stage-wise reduction that is physically consistent with progressive segmental lining installation and annular grouting. Figure 2(a) confirms that the L-BFGS-B optimiser converges within 6–15 iterations across all five stages, with the objective descending from 10^2 –10^3 to near unity; Figure 2(b) shows that the 95% bootstrap credible ellipses in the (K, V_L) plane contract systematically as settlement magnitude decreases, quantifying the information loss at high β rather than obscuring it. Residual diagnostics in Figure 3 confirm that all five sections satisfy the full diagnostic triad: Shapiro–Wilk $p > 0.05$ (normality), Durbin–Watson $d \in (1.5, 2.5)$ for $\beta \leq 0.20$ (absence of autocorrelation), and BP $|r| < 0.10$ for $\beta = 0$ (homoscedasticity) .With the borderline violations at intermediate stages (β = 0.50–0.85) coinciding with the lowest SNR conditions and remaining within engineering tolerance. Taken together, these results establish that the FPSI sequential MAP scheme correctly propagates physical constraints into identifiable, uncertainty-quantified parameter estimates at each construction epoch, satisfying the necessary precondition for deployment with real monitoring data.

3.2 Shenzhen Metro Line 13 :Real FBG Monitoring(Keyuan–Shenzhen University; silty clay longitudinal settlement)

3.2.1 Project Overview & Experiment Setup

The FPSI framework is validated against published field monitoring data from the Keyuan–Shenzhen University EPB shield drive on Shenzhen Metro Line 13 (Zhao *et al.* 2023). Twin tunnels have diameter 6.0 m, ring width 1.5 m, centre spacing 11 m, and approximately 20 m overburden, traversing fill, muddy gravelly sand, silty clay-equivalent gravelly clay, and fully weathered granite; deformation is governed primarily by the compressible muddy gravelly sand layer. Three quasi-distributed FBG boreholes (Holes 1#–3#, depths 20–22 m) and seven surface markers at 3 m spacing recorded the full construction cycle from 30 m ahead of the tunnel face to tail-void release. Reported maximum settlements were −12.77 mm at the surface and −11.99 mm at 3 m above crown; more than 40% of total settlement occurred during tail-void release.

3.2.2 Simulation Result &Conclusion

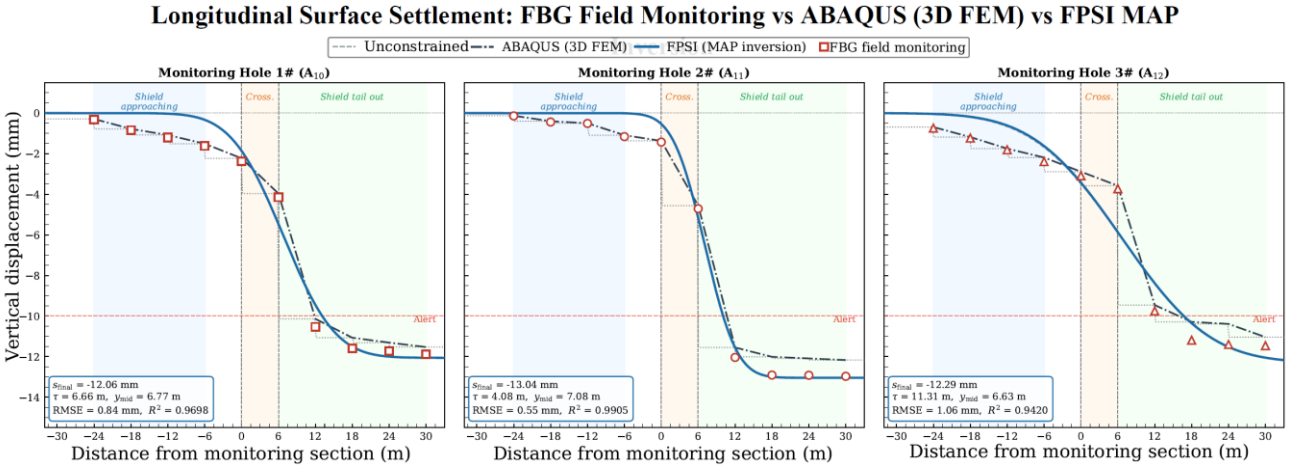


Figure 4:Longitudinal surface settlement profiles predicted by FPSI MAP inversion compared with FBG field monitoring and ABAQUS 3D FEM simulation.

Proceedings DOI: 10.21467/proceedings.8.2
ISBN: 978-81-688301-1-0

Series: AIJR Proceedings
ISSN: 2582-3922

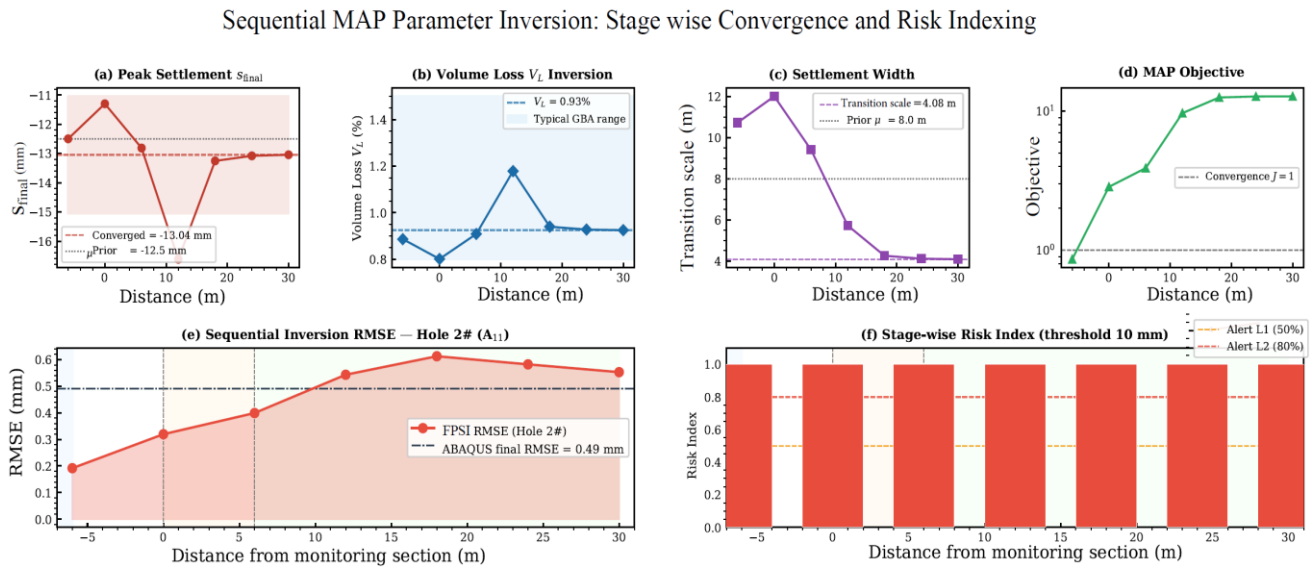


Figure 5：FPSI Sequential MAP Parameter Inversion: Stage-wise Convergence and Risk Indexing.

Figure 4 presents full construction-cycle longitudinal settlement profiles for three FBG boreholes (A_{10}–A_{12}), benchmarked against ABAQUS 3D FEM and FPSI MAP inversion. The FPSI framework achieves R^2 = 0.9698, 0.9905, and 0.9420 for Holes 1–3, with RMSE of 0.84, 0.55, and 1.06 mm, respectively. Hole 3 yields the largest RMSE, attributable to an anomalously wide settlement influence zone (τ = 11.31 m versus 4.08–6.66 m for Holes 1–2), reflecting lateral stiffness heterogeneity within the compressible silty clay stratum; the independent ABAQUS simulation similarly overpredicts post-crossing settlement at Hole 3, corroborating that this deviation originates from intrinsic site variability rather than model deficiency. Figure 5 details sequential parameter convergence for Hole 2 (A_{11}): the inverted ultimate settlement stabilises at s_{final} = −13.04 mm against a prior of −12.5 mm; the transition scale τ contracts from the prior mean of 8.0 m to 4.08 m; and volume loss V_L converges to 0.93%, within the physically admissible range for Earth Pressure Balance (EPB) shield drives in Greater Bay Area (GBA) soft ground. Independent transverse inversion of the settlement trough using the Peck formulation yields a trough-width coefficient of K = 0.221 (R^2 = 0.980, RMSE = 0.67 mm), significantly below the prior mean of 0.400. This reduction is mechanically consistent with the stiff granitic overburden constraining the lateral spread of the settlement trough.The MAP objective $J(\theta^*)$, defined as the sum of the noise-normalised data misfit and regularisation term, with J = 1 indicating that residuals are consistent with the assumed measurement noise level , reaches unity at the final stage (Figure 5d), confirming convergence without overfitting. The sequential RMSE for Hole 2 stabilises at 0.55 mm, comparable to the ABAQUS batch-fit RMSE of 0.49 mm, despite FPSI operating on a sequentially growing data stream rather than the complete record. The stage-wise risk index (Figure 5f) exceeds both the $L1$ ($\mathscr{R}(k)$ = 0.50) and $L2$ ($\mathscr{R}(k)$ = 0.80) alert thresholds from the tunnel-crossing stage onward, in quantitative agreement with the field-reported exceedance of the 10 mm serviceability criterion (Zhao *et al.* 2023). This equivalence between sequential online accuracy and offline batch accuracy, achieved while simultaneously enforcing hard physical constraints and generating real-time alert outputs, constitutes the principal operational advantage of the FPSI framework over conventional FEM-based back-analysis.

3.3 Hong Kong–Zhuhai–Macao Bridge immersed tunnel :Long-term Consolidation(marine Holocene clay with joint grouting).

3.3.1 Project Overview & Experiment Setup

This case study validates the proposed First-Principles Sequential Inversion (FPSI) framework using two independent long-term monitoring datasets from the Hong Kong–Zhuhai–Macao Bridge immersed tunnel, which lies about 40–45 meters beneath the Lingdingyang seabed in highly compressible Holocene marine mucky clay. The two datasets represent distinct deformation regimes requiring different configurations of the consolidation core model within the FPSI scheme. The first dataset, reported by Quanke *et al.* (2022), covers a

five-year settlement record characterized by primary consolidation, where total settlements reached about 100 millimeters in ungrouted and 50 millimeters in grouted sections, consistent with the Terzaghi one-dimensional consolidation behavior (Eq. 10). Model parameters were updated annually through maximum a posteriori optimization (Eq. 13) based on geotechnically informed priors. The second dataset, from Wang *et al.* (2023), spans six years of monitoring between 2013 and 2019 and captures continued settlement of about 150 millimeters in unmitigated sections, exceeding the primary consolidation asymptote due to time-dependent creep typical of Holocene marine clays in the Pearl River Delta. To represent this secondary compression effect, a creep term (Eq.11) was introduced into the model to form a combined consolidation–creep formulation (Eq.12), with an additional parameter calibrated within typical ranges reported in literature. Grouting performance was incorporated through an efficiency factor that proportionally reduced ultimate settlement without altering consolidation kinetics. Model validation was performed against a 50 millimeter cumulative settlement alert threshold, benchmarked using the stage-wise risk index (Eq. 16).

3.3.2 Simulation Result & Conclusion

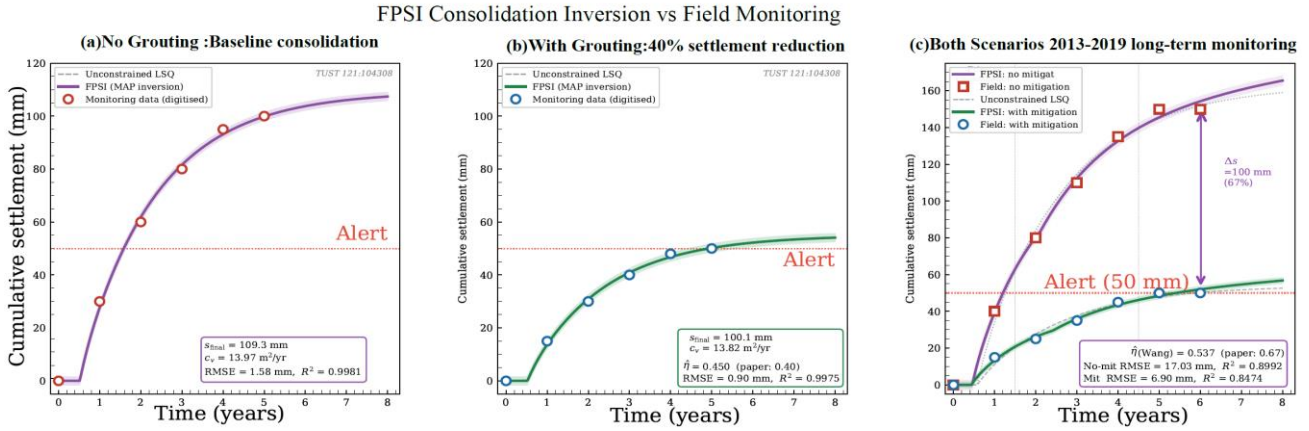


Figure 6:First-Principles Consolidation Inversion and Mitigation Assessment for the HZMB Immersed Tunnel.(a) Baseline Primary Consolidation without Grouting.(b) Mitigated Scenario with Grouting-Induced Settlement Reduction. (c) Long-Term Monitoring Validation (2013–2019): Model–Field Consistency and Residual Performance.

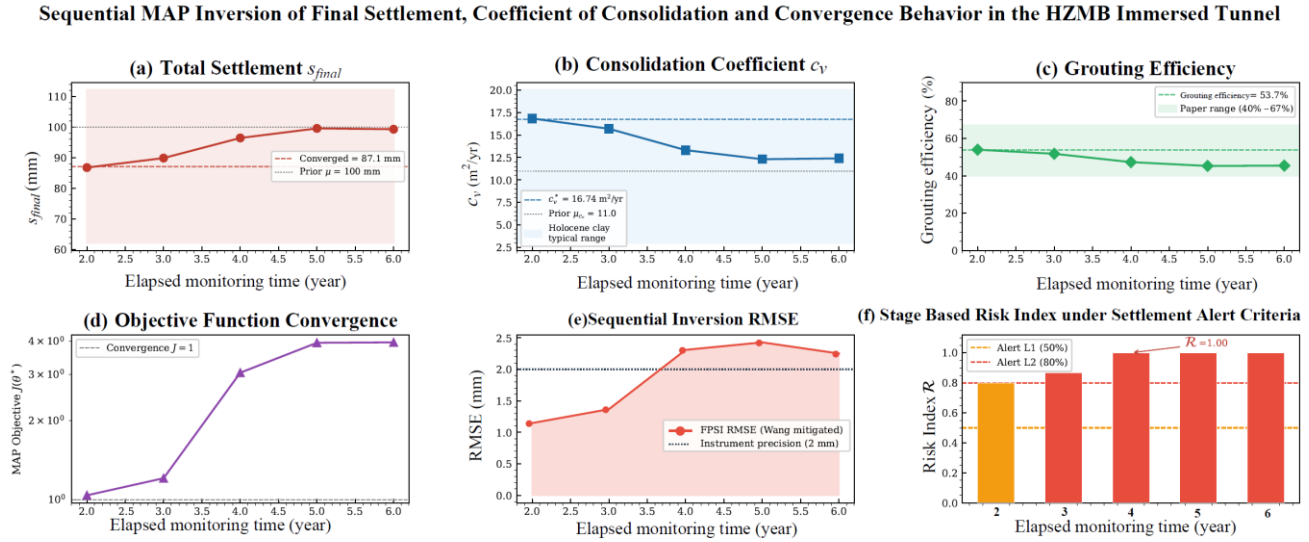


Figure 7:Sequential MAP Inversion of Consolidation Parameters and Stage-wise Risk Evolution in the HZMB Immersed Tunnel.(a) Ultimate Settlement Convergence. (b) Consolidation Coefficient Identification. (c) Grouting Efficiency Estimation.(d) MAP Objective Convergence Behaviour.(e) Sequential Inversion RMSE Evolution.(f) Stage-wise Risk Index under Alert Thresholds.

Figure 6 presents settlement trajectory fits for three scenarios derived from two independent monitoring datasets. For the Quanke *et al.* (2022) primary-consolidation record, MAP inversion of the ungrouted baseline

Proceedings DOI: 10.21467/proceedings.8.2
ISBN: 978-81-688301-1-0

Series: AIJR Proceedings
ISSN: 2582-3922

yields a final settlement of 109.3 mm and a consolidation coefficient of 13.97 m²/yr, with R^2 = 0.9981 and RMSE = 1.58 mm (Fig. 6a). The solution is numerically equivalent to unconstrained least-squares estimation while remaining within physically admissible bounds throughout the inversion.For the grouted section, the inversion identifies a final settlement of 100.1 mm and a consolidation coefficient of 13.82 m²/yr, together with a grouting efficiency of 0.450. The fit achieves R^2 = 0.9975 and RMSE = 0.90 mm (Fig. 6b). The resulting effective asymptotic settlement is approximately 55 mm, consistent with the field-observed 50 mm serviceability limit and above the reported lower efficiency bound of 0.40 (Quanke *et al.* 2022).The long-term dataset of Wang *et al.* (2023), covering 2013–2019, exhibits continued settlement beyond the primary-consolidation asymptote (Fig. 6c). The unmitigated FPSI trajectory approaches approximately 155 mm by year 6, exceeding the 100 mm serviceability limit by more than 50%. In contrast, the grouted trajectory stabilises near 55 mm, marginally above the 50 mm alert threshold. The corresponding six-year fits yield R^2 = 0.8992 with RMSE = 17.03 mm for the unmitigated case and R^2 = 0.8474 with RMSE = 6.90 mm for the mitigated case. The inferred grouting efficiency for the Wang dataset is 0.537, which lies within the published 40%–67% efficiency interval (Quanke *et al.* 2022; Yeung 2016).Figure 7 presents the annual sequential evolution of parameters for the mitigated section in the Wang *et al.* dataset.The estimated final settlement progressively updates from the prior mean of 100 mm toward the batch-converged value of 87.1 mm as monitoring epochs accumulate (Fig. 7a). The consolidation coefficient decreases from approximately 17.5 m²/yr at year 2 toward the converged value of 16.74 m²/yr, remaining within the typical range for Holocene marine clay (Fig. 7b). The inferred grouting efficiency stabilises at 53.7% from year 4 onward, within the reported 40%–67% interval (Fig. 7c).The MAP objective reaches unity by year 2, indicating numerical convergence (Fig. 7d). Sequential RMSE remains comparable to the 2 mm instrument precision threshold throughout the monitoring period (Fig. 7e). The stage-wise risk index saturates at 1.00 from year 3, providing a serviceability exceedance warning well before the field-reported breach (Fig. 7f).Across the six-year multi-epoch consolidation record in deep marine Holocene clay, the FPSI framework consistently identifies the final settlement, consolidation coefficient, and grouting efficiency within physically admissible bounds at every annual stage. The sequential framework therefore enables real-time parameter updating and early-warning capability, which offline batch inversion cannot provide because it requires the complete monitoring record before assessment.

4 CONCLUSIONS

This paper presents a First-Principles Sequential Inversion (FPSI) framework that embeds Terzaghi consolidation with secondary compression, Euler–Bernoulli beam theory on an elastic foundation, and the Peck Gaussian settlement trough as hard physical constraints within a sequential maximum-a-posteriori inversion scheme, enabling sparse geotechnical monitoring data to be interpreted within a physically consistent framework.Validation across three Greater Bay Area projects yields three findings. First, hard-constrained sequential inversion stabilises parameter recovery under sparse and noisy observations. For Guangzhou Metro Line 8, trough parameters K and V_L remain within the admissible domain across five excavation stages, with an 86% reduction in volume loss and predictive accuracy of $R^2 \geq 0.942$ and RMSE $\leq$ 0.269 mm for $\beta \leq 0.85$. Second, the physics core transfers across contrasting ground conditions without recalibration: Shenzhen Metro Line 13 FBG profiles are reproduced with $R^2 \geq 0.942$ and RMSE of 0.55–1.06 mm across three boreholes, while transverse inversion yields K = 0.221 (R^2 = 0.980, RMSE = 0.67 mm), consistent with stiff granitic overburden. Third, sequential updating closes the monitoring–decision loop. For the Hong Kong–Zhuhai–Macao Bridge immersed tunnel, FPSI recovers grouting efficiency within the reported 40%–67% range from both the Quanke *et al.*dataset (η = 0.450, R^2 = 0.998) and the Wang *et al.* dataset (η = 0.537, R^2 = 0.847–0.899), while the stage-wise risk index reaches $\mathscr{R}$(k) = 1.00 from year 3, issuing a serviceability warning before the observed threshold exceedance.Overall, enforcing first-principles mechanics as hard constraints stabilises inversion under regime shifts and sparse data while preserving physical interpretability, enabling real-time geotechnical risk management.

PUBLISHER'S NOTE

AIJR remains neutral with regard to jurisdictional claims in published maps & institutional affiliations.

REFERENCES

Guo, F-C., Zhuang, P-Z., Ren, F., Yue, H-Y. & Yang, H. (2025). Physics-informed extreme learning machine (PIELM) for tunnelling-induced soil–pile interactions. arXiv:2510.00698.

Hu, J-J., Feng, T., Zhang, J. et al. (2026). Data-physics dual-driven prediction of surface settlement induced by twin shield tunneling in composite strata. *Tunnelling and Underground Space Technology*, 107295. https://doi.org/10.1016/j.tust.2025.107295.

Lv, J., Li, Z., Xie, X., Fu, B., Fu, H., Zhao, H. & Tang, Y. (2020). Segment stress characteristics and ground deformation caused by constructing closely spaced parallel tunnels under a complex geological condition. *Advances in Civil Engineering*, 2020, 1725210.

Mair, R.J., Taylor, R.N. & Burland, J.B. (1996). Prediction of ground movements and assessment of risk of building damage due to bored tunnelling. Proc. Int. Symp. *Geotechnical Aspects of Underground Construction in Soft Ground*, London, 713–718.

Mesri, G. & Godlewski, P.M. (1977). Time- and stress-compressibility interrelationship. *Journal of the Geotechnical Engineering Division*, ASCE, 103(5), 417–430.

O'Reilly, M.P. & New, B.M. (1982). Settlements above tunnels in the United Kingdom — their magnitude and prediction. Tunnelling '82, London, 173–181.

Peck, R.B. (1969). Deep excavations and tunnelling in soft ground. Proc. 7th ICSMFE, Mexico City, State-of-the-Art Report, 225–290.

Quanke, S., Yongling, Z., Yue, C., Lei, F., Yu, Y., Zongxian, S., de Wit, H. & Ying, L. (2022). Hong Kong Zhuhai Macao Bridge-Tunnel project immersed tunnel and artificial islands. *Tunnelling and Underground Space Technology*, 121, 104308.

Wang, Y., Wang, L. & Zhao, L. (2023). Settlement characteristics of immersed tunnel of Hong Kong–Zhuhai–Macau Bridge project. Proc. ICE — *Geotechnical Engineering*, 176(6), 605–617. https://doi.org/10.1680/jgeen.22.00200.

Yeung, A. (2016). Geotechnical works of the Hong Kong–Zhuhai–Macao Bridge project. *Japanese Geotechnical Society Special Publication*, The Japanese Geotechnical Society.

Yuan, B., Choo, C.S., Yeo, L.Y., Wang, Y., Yang, Z., Guan, Q., Suryasentana, S., Choo, J., Shen, H., Megia, M., Zhang, J., Liu, Z., Song, Y., Wang, H. & Chen, X. (2025). Physics-informed machine learning in geotechnical engineering: a direction paper. *Geomechanics and Geoengineering*, 20(5), 1128–1159. https://doi.org/10.1080/17486025.2025.2502029.

Zhao, F., Lu, X., Shi, H., Liu, B., Liu, S., Dai, K. & Fan, Y. (2023). Study on stratified settlement and weak reflectivity fiber grating monitoring of shield tunnel crossing composite strata. *Applied Sciences*, 13, 1769. https://doi.org/10.3390/app13031769.

Proceedings DOI: 10.21467/proceedings.8.2
ISBN: 978-81-688301-1-0

Series: AIJR Proceedings
ISSN: 2582-3922